STRUCTURAL SCIENCE
CRYSTAL ENGINEERING
MATERIALS

Volume 78 (2022)

Supporting information for article:

Size–strain line-broadening analysis of anatase/brookite (TiO2)-based nanocomposites with carbon (C): PXRD and Raman spectroscopic analysis

Aleksandar Kremenović, Mirjana Grujić-Brojčin, Nataša Tomić, Vladimir Lazović, Danica Bajuk-Bogdanović, Jugoslav Krstić and Maja Šćepanović

S1. TGA

The loading percentage of C in TiO_2 for T-C9 and T-C20 is calculated from TGA curves. The prompt decrease around 600 °C on TGA curves, as shown in Figure S1, corresponds to release of CO_2 (Sun *et al.*, 2014; Cong *et al.*, 2015), providing the information about the carbon content (9 and 20% in T-C9 and T-C20, respectively). It should be noted that this carbon content represents both crystalline and amorphous phases of carbon.

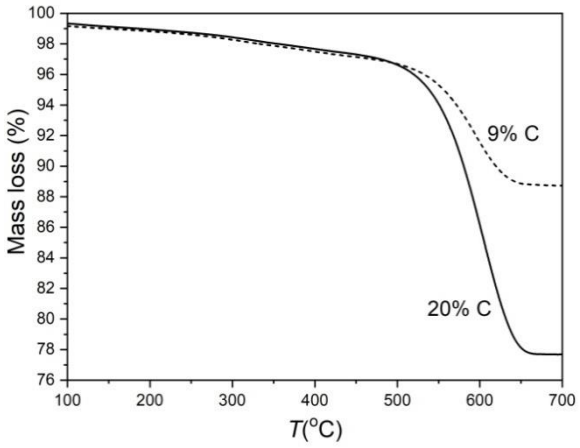

Figure S1 TGA curve of T-C9 and T-C20.

S2. XRPD

S2.1. Method

Structure and microstructure information was obtained *via* Rietveld method (Rietveld, 1969; Rodriguez-Carvajal, 1993, 2001, 2016). Within the Fullprof program suite line profile broadening is implemented via the Thompson-Cox-Hastings modified pseudo-Voigt (TCH-pV) function (Tompson & Hastings., 1987) to account for the isotropic size and strain effects. The apparent size and strain are calculated for each reflection according to Rodriguez-Carvajal (2016) as:

$$\text{Apparent size (Å)} = \frac{1}{\beta_{size}} \text{ (Å)} \qquad \text{(S1)}$$

$$\text{Max-strain} = \frac{\beta_{strain} d_{hkl}}{2} \quad (\text{x}10^{-4}) \qquad \text{(S2)}$$

The strain calculated using Fullprof thus corresponds to 1/4 of the apparent microstrain defined by Stokes & Wilson (1944). It is the so-called maximum (upper limit) microstrain, related by a constant factor to the root-mean-square-microstrain. Both β_{size} and β_{strain} were obtained from TCH-pV functions parameters (isotropic effects) according to the procedure described in (Rodriguez-Carvajal, 2016) while

d_{hkl} is interplanar spacing. The β_{size} was obtained from the size parameter contributing to the full width at half maximum (FWHM):

$$\mathrm{FWHM\,(Lorentzia\,n\,-\,size)} = \mathrm{H_{LZ}} = \frac{Y + S_z}{\cos\theta} \quad \text{(S3)}$$

$$\mathrm{FWHM\ (Gaussian\ \ -\,size)} = \mathrm{H_{GZ}} = \frac{IG}{\cos^2\theta} \quad \text{(S4)}$$

Beta-strain (β_{strain}) is obtained from the strain parameters contributing to the FWHM (Rodriguez-Carvajal, 2016):

$$\mathrm{FWHM^2\ (Gaussian\ \ -\,strain)} = \mathrm{H_{GS}}^2 = [\mathrm{U} + (1-\mathrm{z})^2\,\mathrm{DST}^2]\tan^2\theta \quad \text{(S5)}$$

$$\mathrm{FWHM\ \ (Lorentzia\,n\,-\,strain)} = \mathrm{H_{LS}} = [\mathrm{X} + \mathrm{z\,DST}]\,\tan\theta\,. \quad \text{(S6)}$$

In formulas (S3)-(S6) *Y*, S_z, *IG*, *U*, *DST* and *X* are refinable parameters. The anisotropy of XRPD line broadening was checked but is not evident.

S2.2. XRPD patterns of synthesized samples and standard specimen

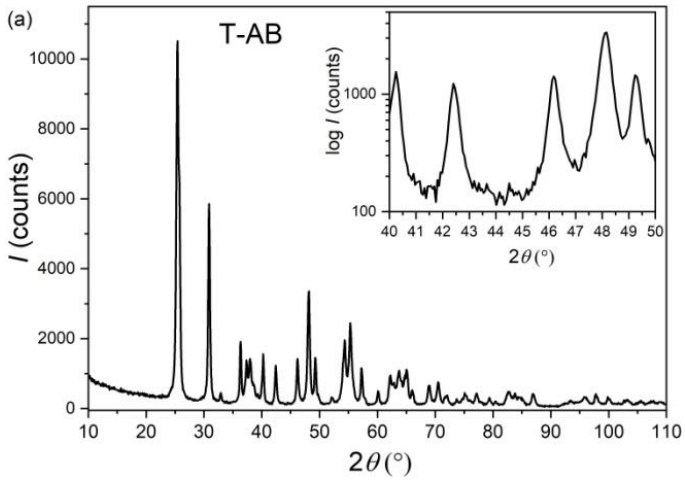

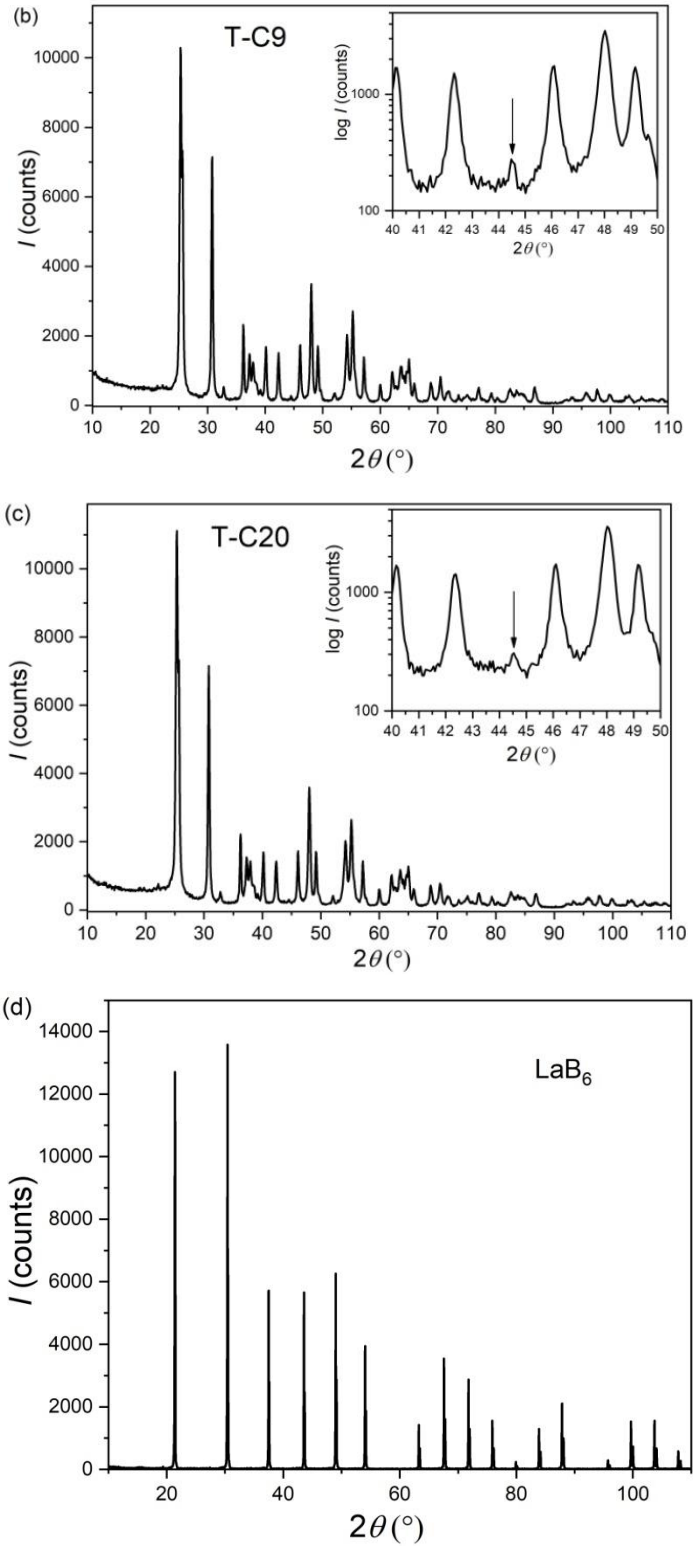

Figure S2 XRPD patterns of synthesized samples: (a) pure T-AB, (b) T-C9, (c) T-C20 and (d) standard specimen LaB_6. The carbon-related region is shown in the Insets, with peaks corresponding to crystalline carbon at about ~44.5 °2θ pointed by the arrow in samples T-C9 and T-C20.

S2.3. XRPD pattern of original carbon black

The XRPD result suggests that untreated carbon black is amorphous to microcrystalline.

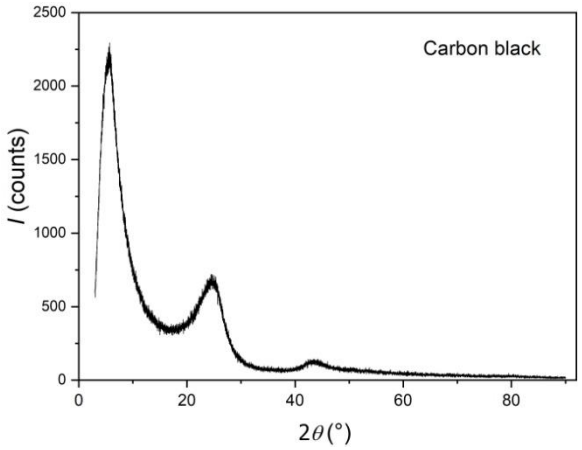

Figure S3 XRPD of carbon black.

S3. Raman scattering

S3.1. Phonon confinement model (PCM)

The PCM is phenomenological method used to simulate experimental Raman spectra in order to take into account different nanosize induced effects (Gouadec & Colomban, 2007). In this model several independent factors, like phonon confinement, strain, non-homogeneity of the size distribution and variations in phonon relaxation with crystallite size decreasing contribute to the changes in the position and linewidth of calculated Raman mode (Richter *et al.*, 1981; Campbell & Fauchet, 1986; Spanier *et al.*, 2001; Šćepanović *et al.*, 2007; Grujić-Brojčin *et al.*, 2009). Due to crystallite size decrease, the phonons are confined and optical phonons over the entire Brillouin zone are contributing to the first-order Raman spectra. The Raman intensity $I(\omega)$, according to Richter *et al.* (1981) and Campbell & Fauchet (1986), for effective crystallite size (or coherence length) L and Gaussian confinement function, is calculated as a superposition of weighted Lorentzian contributions over the whole Brillouin zone:

$$I(\omega) \propto \sum_{i=1}^{n} \int_0^{\infty} \rho(L)dL \int_{BZ} \frac{\exp\left(\frac{-q^2L^2}{8\beta}\right) \mathrm{d}^3q}{\left(\omega - \left(\omega_i(q) + \Delta\omega\right)\right)^2 + \left(\frac{\Gamma}{2}\right)^2} \qquad \text{(S7)}$$

with $\rho(L)$ - crystallite size distribution, q - wave vector, β - confinement strength and Γ - the intrinsic mode linewidth. The Brillouin zone is assumed to be homogeneous and isotropic sphere, and the sum is carried over n dispersion curves $\omega_i(q)$, with mode degeneracy and symmetry of directions in the Brillouin zone taken into account. Phonon dispersions are usually taken from corresponding bulk

counterparts, due to lack of appropriate experimental and theoretical dispersions of nanocrystalline materials (Grujić-Brojčin *et al.*, 2009; Šćepanović *et al.*, 2007). The crystallite size distribution is defined by Gaussian distribution

$$\rho(L) = 1/\sigma\sqrt{2\pi}\cdot\exp\left(-(L-L_0)^2/2\sigma^2\right) \quad \text{(S8)}$$

with L_0 as effective crystallite size (correlation length), and σ as standard deviation, whereas distribution width is given by

$$w = 2\sigma\sqrt{\ln 4}\,. \quad \text{(S9)}$$

Beside the nanocrystallite size, the changes in lattice parameters may affect Raman peak position. This effect was introduced in the PCM for cubic lattice by Spanier et al. (2001), where the additional shift of Raman mode due to relative variation of lattice parameters is given as

$$\Delta\omega(q) = -3\gamma\omega(q)\Delta a/a_0\,. \quad \text{(S10)}$$

where γ represents Grüneisen parameter, $\Delta a/a_0$ - relative variation of unit cell parameter, and a_0 – unstrained unit cell parameter. However, this approach may not be the most appropriate for non-cubic lattices; according to the procedure proposed by Kibasomba *et al.* (2018), based on the relations of Gouadec and Colomban (2007), the additional shift $\Delta\omega$ of Raman mode due to so-called Raman strain ε_R may be defined:

$$\Delta\omega = -\omega_0\frac{a+r+3}{2}\varepsilon_R\,, \quad \text{(S11)}$$

where ω_0 is the frequency of Raman mode in unstrained bulk crystal, a and r are the constants related to attractive and repulsive contributions, respectively, in the interatomic potential function. So-called Raman strain, ε_R, represents the tensile or compressive strain in the nanocrystallites, which induces red- or blue-shift of the Raman modes ($\Delta\omega$), respectively. According to authors mentioned above, in case of TiO_2 only covalent bonds may be taken into account and the contribution of Raman strain to Raman shift may be expressed by

$$\Delta\omega = -3\omega_0\varepsilon_R\,. \quad \text{(S12)}$$

Anatase E_g modes in T-AB, T-C9 and T-C20 are simulated by using the following room temperature parameter set: the phonon strength β=9, intrinsic linewidth Γ=8.5 cm^{-1}, (Šćepanović *et al.*, 2007; Grujić-Brojčin *et al.*, 2009), Grüneisen parameter γ=2.85 (Hearne *et al.*, 2004; Wang *et al.*, 2007), V_0 =136.26 $Å^3$ (Horn *et al*., 1972), and phonon dispersion function taken in cosine form (Mikami *et al.*, 2002; Grujić-Brojčin *et al.*, 2009) with the frequency of the E_g mode in Γ point at ω_0=143.5 cm^{-1} (Šćepanović *et al.*, 2007). The integration has been performed along the high-symmetry G-X direction of the Brillouin zone (Šćepanović *et al.*, 2007; Grujić-Brojčin *et al.*, 2009).

S3.2. Raman results on TiO_2 based nanocomposites with different carbon content

The Raman spectra of pure (T-AB) and titania based nanocomposites with carbon content of 0.3, 1, 4, 9, and 20 % (samples T-C0.3, T-C1, T-C4, T-C9, and T-C20, respectively) are shown in Figure S4(a). The Raman spectra of all synthesized samples are dominated by Raman features of anatase (Ohsaka *et al.*, 1978; Šćepanović *et al.*, 2007) and brookite (Iliev *et al.*, 2013; Tomić *et al.*, 2015) crystalline phases. To estimate the contribution of anatase (E_g) and brookite (A_{1g}) modes to the most intense Raman feature centred at 144-150 cm^{-1}, the part of the spectra in the region of 100-200 cm^{-1} are shown on an enlarged wavenumber scale (Figure S4(b)). Also, the part of the spectra in the region 200-800 cm^{-1} is shown on an enlarged intensity scale, in order to enhance visibility of the anatase and, especially, brookite modes of lower intensity (Figure S4(c)).

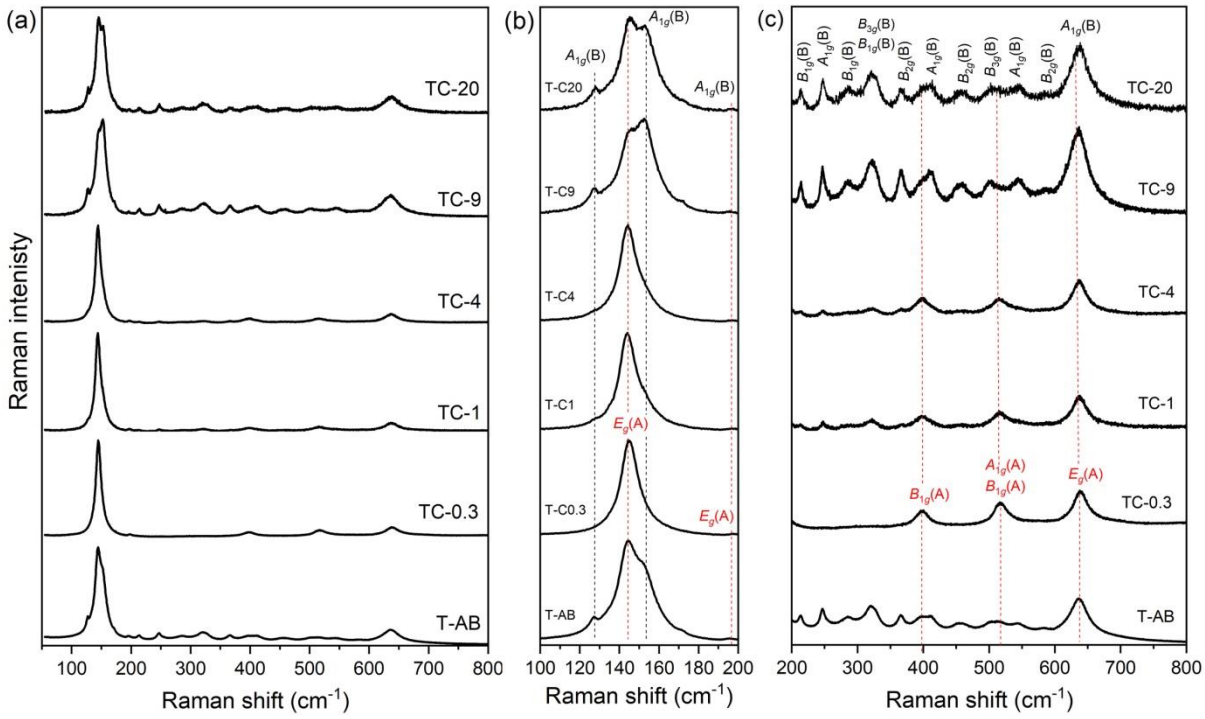

Figure S4 (a) The Raman spectra of pure (T-AB) and titania nanocomposites with carbon content from 0.3 to 20 % (samples T-C0.3 to T-C20). (b) Part of the spectra in the anatase-brookite fingerprint region shown on an enlarged wavenumbers scale. (c) The spectra in the region 200-800 cm^{-1} shown with enlarged intensity scale. Anatase and brookite modes denoted by (A) and (B), respectively.

Broad Raman feature at about ~148 cm^{-1} in the Raman spectrum of pure titania (T-AB) originates from anatase E_g mode at ~ 145 cm^{-1} and several brookite modes, among which the most intense is A_{1g} mode at ~ 153 cm^{-1}. Although the brookite content in this sample is predominant, and according to XRPD results is about 74 % (see the main text of the article), the anatase E_g mode is more intense than A_{1g} brookite mode, due to much higher Raman scattering efficiency of anatase in comparison to brookite phase. However, the spectrum of TiO_2 based nanocomposite sample T-C0.3 with small content of carbon is fully dominated by anatase Raman modes, with very small contributions of brookite modes.

According to these results, it seems that adding small amount of carbon together with hydrogel to autoclave favours the creation of the anatase phase in produced nanocomposite. With increasing carbon content the intensity of brookite Raman modes increases so that A_{1g} brookite mode at ~ 153 cm^{-1} becomes the most intense mode in the spectrum of nanocomposite sample T-C9 with 9 % of carbon content (Figure S4(b)), and other brookite modes also increase their intensity (Figure S4(c)). Note that according to XRPD results brookite content in this sample is about 83 %. However, in the spectrum of the sample T-C20 with 20% carbon, anatase E_g mode becomes again the most intensive, which is in line with the XRPD results, which show that brookite amount (77 %) in this sample is less than in the sample T-C9.

S4. Brookite to anatase amount ratio – XRPD and Raman spectroscopy

The XRPD and Raman scattering measurements also provide the information on anatase to brookite content ratio, as shown in Figure S5. Note that Raman scattering gives the information on relative variation of phase content ratio in the sample series by using the ratio of integrated intensities of the most intensive brookite (A_{1g}) and anatase (E_g) Raman mode, where lower Raman scattering efficiency of brookite in comparison to anatase leads to the values of modes intensity ratio considerably lower than real phase content ratio.

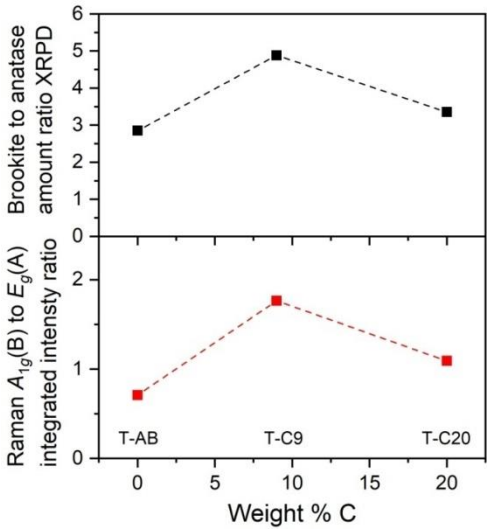

Figure S5 The dependence of brookite to anatase amount ratio obtained from XRPD and the integrated intensity ratio of most intensive brookite to anatase Raman mode in T-AB, T-C9 and T-C20.

S5. FTIR

The FTIR spectra of pure TiO_2 (T-AB) and nanocomposites T-C9 and T-C20 are shown in Figure S6. The bands close to 3400 cm^{-1} and 1630 cm^{-1} in the spectrum of T-AB (Figure S6(a)) are assigned to the stretching vibration of hydroxyl groups and bending vibrations of H_2O molecules, respectively. These vibrations are not detected in FTIR spectra of nanocomposites (Figure S6(b, c)). Furthermore, the presence of CH and CO bands in the FTIR spectra of the samples TiO_2 with 9% C and TiO_2 with 20% C weren't detected.

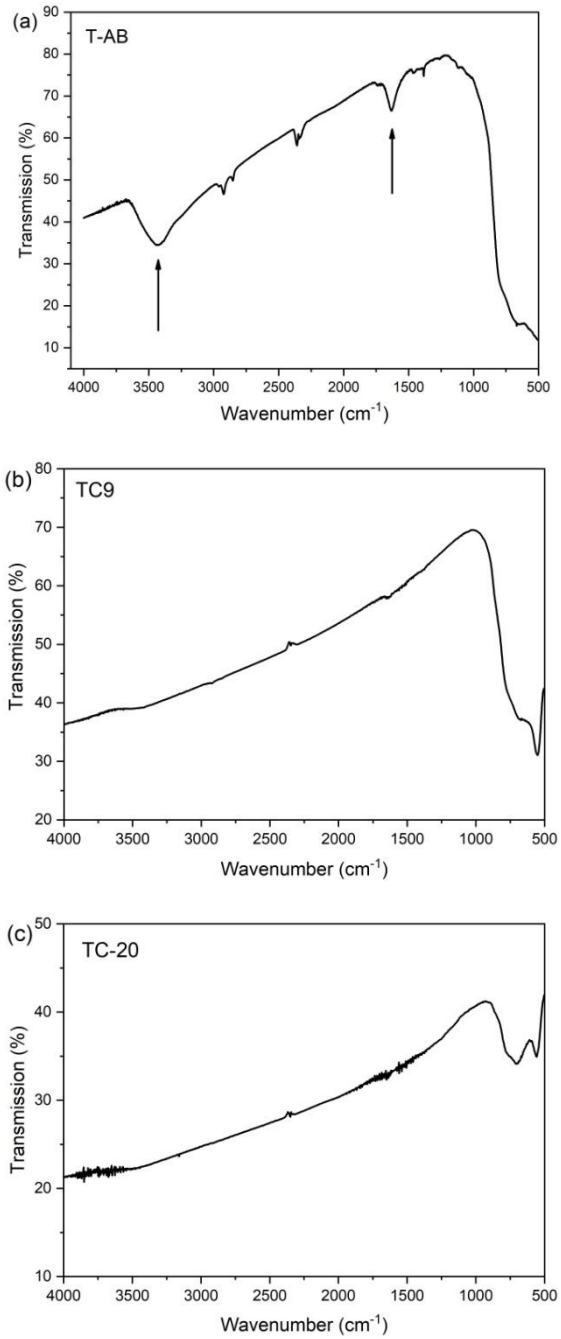

Figure S6 IR transmission spectra of (a) T-AB, (b) TC-9 and (c) TC-20 nanopowder.

S6. SEM

The SEM images of T-AB and T-C20 nanopowder samples are presented in Figure S7. Two different types of particles are noticed in both samples: spherical, ascribed to anatase and spindle like particles, characteristic for brookite (Tomić *et al*., 2015). In general, there is no significant difference in powder morphology, which might be expected, having in mind similar anatase to brookite content ratio in those samples. In T-C20 the shape of particles is retained in comparison to T-AB, with certain agglomeration of both anatase and brookite.

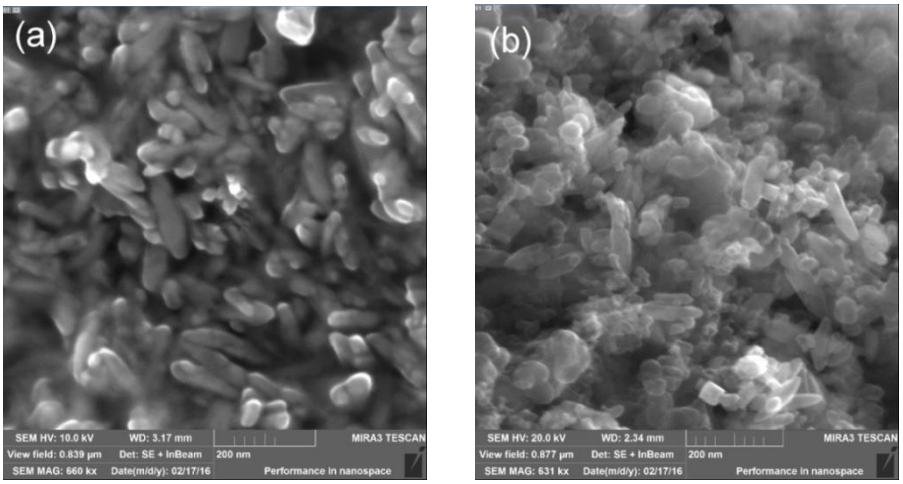

Figure S7 SEM image of T-AB and T-C20.

S7. Nitrogen physisorption at 77 K

The adsorption-desorption isotherms of these samples are presented in Figure S8(a). The isotherms of examined materials correspond to type II (Roquerol *et al.*, 1994), characteristic for poorly porous materials. In this case, the presence of hysteresis loop in region of high value of relative pressures (p/p_0> 0.8) can be noticed. This is a consequence of weakly bonded agglomerate system, and leads to an interparticle porosity.

Based on nitrogen physisorption measurements at 77 K in region $p/p_0 < 0.30$ specific surface area (S_{BET}) of samples T-AB, T-C9 and T-C20 is calculated from the linear part of the adsorption isotherm by applying the Brunauer-Emmet-Teller (BET) equation (Brunauer *et al.* 1938). Values are presented in Table S1. Information regarding the total pore (V_{tot}), mesopore (V_{meso}) and micropore (V_{mic}) volumes were also summarized in Table S1. The total pore volume was obtained from the N_2 adsorption, expressed in liquid form, by using the Gurvitsch rule (Gregg *et al.* 1982). The micropore volume has

been estimated by the Dubinin - Radushkevich (Dubinin, 1975). The mesopore volume, as well as mesopore size distribution have been estimated by the Barrett-Joyner-Halenda (BJH) method from the desorption branch of the isotherms (Barret *et al.*, 1951). The value of the most frequent pore diameter (D_p) for all samples (T-AB, T-C9 and T-C20) is evaluated by BJH (Barret *et al.*, 1951) method, using the desorption branch of isotherm curves. Furthermore, the pore size distributions, given in Figure S8(b), represent actually distribution of interparticle space of examined nanopowders.

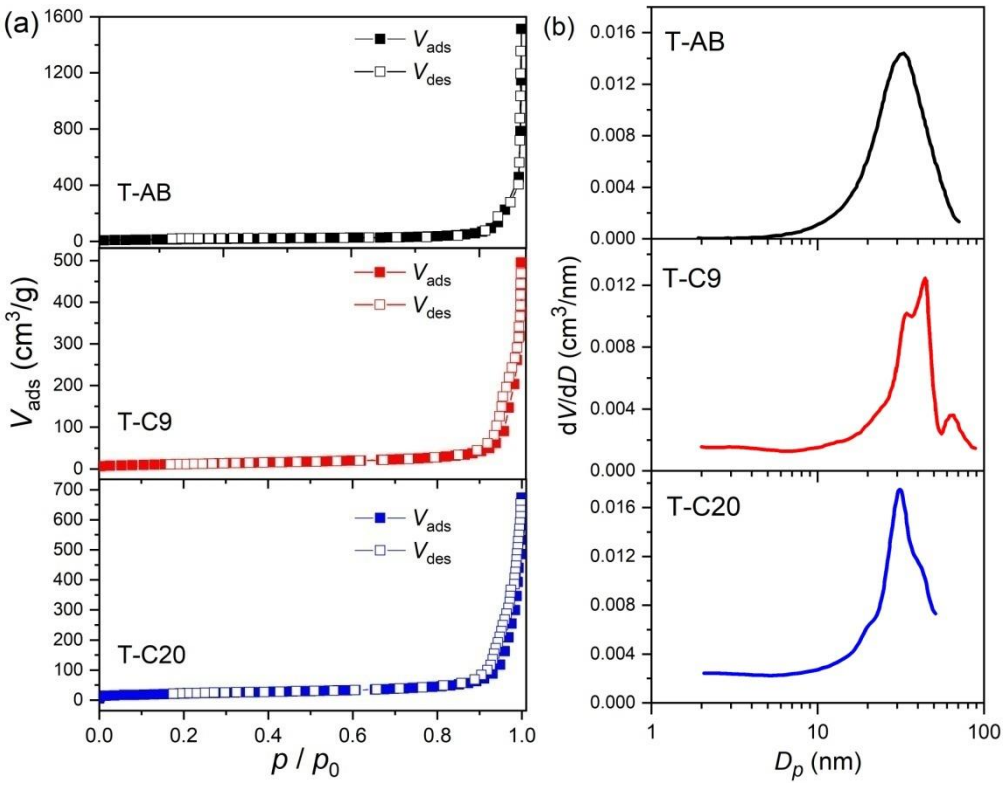

Figure S8 **(**a) Nitrogen physisorption at 77 K and (b) pore size distribution for pure T-AB, and nanocomposites TC-9 and T-C20.

Table S1 Specific surface area(S_{BET}), total pore, mesopore and micropore volumes (V_{tot}, V_{meso}, V_{mic}) and the most frequent pore diameter (D_p) for T-AB, T-C9 and T-C20 samples.

Sample	S_{BET} (m^2/g)	V_{tot} (cm^3/g)	V_{meso} (cm^3/g)	V_{mic} (cm^3/g)	D_p(nm)
T-AB	58.6	0.564	0.346	0.018	32.2
TC-9	43.5	0.292	0.286	0.014	44.2
TC-20	76.8	0.428	0.406	0.028	31.1

According to these results, the T-C20 sample has a 30% higher specific surface area compared to the one of the pure TiO_2, whereas theT-C9 sample has specific surface area that is almost 25% lower than

the one of the pure TiO_2. Having in mind that BET specific surface area (S_{BET}) for the carbon black is 239 m^2/g, it is reasonable to assume that the formation of two composites is taking place in a different manner.

References

Barrett, E.P., Joyner, L.G., Halenda, P.P. (1951) *J. Am. Chem. Soc.* **73** (1951) 373.

Campbell, I.H. &Fauchet, P.M. (1986) *Solid State Commun.***58**, 739–441.

Dubinin, M.M. (1975) *Progress in Surface and Membrane Science* **9** (1975) 1-70.

Gregg, S.J. & Sing, S.J. (1982) *Adsorption, Surface Area and Porosity* (Academic Press, London).

Grujić-Brojčin, M., Šćepanović,M. J., Dohčević-Mitrović, Z. D. &P opović, Z. V. (2009) *Acta Phys. Pol. A***116**, 51-54.

Hearne, G. R., Zhao, J., Dawe, A. M., Pischedda, V., Maaza, M., Nieuwoudt, M. K., Kibasomba, P., Nemraoui, O., Comins, J. D. &Witcomb, M. J. (2004) *Phys. Rev. B***70**, 134102.

Mikami, M., Nakamura, S., Kitao, O. &Arakawa, H. (2002) *Phys. Rev. B***66**, 155213(1-6).

Richter, H., Wang, Z.P.& Ley, L. (1981) *Solid State Commun.***39**, 625–629.

Rodriguez-Carvajal, J. (1993) *Physica B* **192**, 55–69.

Rodríguez-Carvajal, J. (2001) *Recent Developments of the Program FULLPROF, in Commission on Powder Diffraction (IUCr) Newsletter***26**, 12–19. (http://journals.iucr.org/iucr-top/comm/cpd/Newsletters/)

Rodriguez-Carvajal, J. (2016) FullProf computer program (https://www.ill.eu/sites/fullprof/)

Spanier, J. E., Robinson, R. D., Zhang, F., Chan, S.-W.& Herman, I. P.(2001) *Phys. Rev. B***64**, 245407(1–8).

Stokes A. R. & Wilson A. J. C. (1944) *Proc. Phys. Soc. London* **56**, 174–181.

Tompson, P., Cox D.E. & Hastings J. M. (1987) *J. Appl. Cryst.*, **20**, 79–83.

Wang, D., Chen, B., & Zhao, J. (2007) *J. Appl. Phys.* **101**, 113501.